Earth and Planetary Science Letters 305 (2011) 413–424

Contents lists available at ScienceDirect

Earth and Planetary Science Letters

journal homepage: www.elsevier.com/locate/epsl

Heterogeneous plate locking in the South–Central Chile subduction zone: Building up the next great earthquake

M. Moreno [a,*], D. Melnick [b], M. Rosenau [a], J. Bolte [c], J. Klotz [a], H. Echtler [a,b], J. Baez [d], K. Bataille [d], J. Chen [a], M. Bevis [e], H. Hase [f], O. Oncken [a]

[a] Helmholtz Centre Potsdam, GFZ German Research Centre for Geosciences, Germany
[b] Institut für Erd- und Umweltwissenschaften, Universität Potsdam, Germany
[c] Zentrum für Astronomie und Astrophysik, Technische Universität Berlin, Germany
[d] Universidad de Concepción, Chile
[e] School of Earth Science, Ohio State University, OH, USA
[f] Bundesamt für Kartographie und Geodäsie, Geodetic Observatory TIGO, Concepción, Chile

ARTICLE INFO

Article history:
Received 23 September 2010
Received in revised form 11 March 2011
Accepted 15 March 2011
Available online 8 April 2011

Editor: P. Shearer

Keywords:
GPS
Chile
Maule
locking degree
postseismic deformation
earthquake cycle

ABSTRACT

We use Global Positioning System (GPS) velocities and kinematic Finite Element models (FE-models) to infer the state of locking between the converging Nazca and South America plates in South–Central Chile (36°S − 46°S) and to evaluate its spatial and temporal variability. GPS velocities provide information on earthquake-cycle deformation over the last decade in areas affected by the megathrust events of 1960 (M_w = 9.5) and 2010 (M_w = 8.8). Our data confirm that a change in surface velocity patterns of these two seismotectonic segments can be related to their different stages in the seismic cycle: Accordingly, the northern (2010) segment was in a final stage of interseismic loading whereas the southern (1960) segment is still in a postseismic stage and undergoes a prolonged viscoelastic mantle relaxation. After correcting the signals for mantle relaxation, the residual GPS velocity pattern suggests that the plate interface accumulates slip deficit in a spatially and presumably temporally variable way towards the next great event. Though some similarity exist between locking and 1960 coseismic slip, extrapolating the current, decadal scale slip deficit accumulation towards the ~300-yr recurrence times of giant events here does neither yield the slip distribution nor the moment magnitude of the 1960 earthquake. This suggests that either the locking pattern is evolving in time (to reconcile a slip deficit distribution similar to the 1960 earthquake) or that some asperities are not persistent over multiple events. The accumulated moment deficit since 1960 suggests that highly locked patches in the 1960 segment are already capable of producing a M ~ 8 event if triggered to fail by stress transfer from the 2010 event.

1. Introduction

Plate tectonic strain accumulation and release take place at the highest rates along subduction zones which produce the largest earthquakes on Earth. Elastic strain energy that builds up over tens or hundreds of years is partly or totally released by dip-slip earthquakes on the shallow part (<50 km depth) of the subduction plate interface. The rate of stress accumulation on the megathrust may be both temporally variable (e.g., Prawirodirdjo et al., 2010; Walcott, 1978) and spatially heterogeneous (e.g., Chlieh et al., 2008; Moreno et al., 2010; Perfettini et al., 2010). The heterogeneity of the interface locking may correlate with rupture zones of historical megathrust events (e.g., Bürgmann et al., 2005) but also may be controlled by geological variations along the upper plate (e.g., Song and Simons, 2003; Wells et al., 2003) as well as by geometrical/rheological properties of the plate interface. The latter seem to control coseismic slip distributions in the form of barriers and asperities (Kanamori, 1986) along the subduction plate interfaces, their temporal variability and mechanics, however, remain an insufficiently understood topic.

Where information spanning several seismic cycles is available, earthquakes seems to be neither time-predictable (Murray and Segall, 2002) nor slip-predictable (Murray and Langbein, 2006). Candidate mechanisms to introduce variability in seismic cycles are stress transfer from adjacent earthquakes, aseismic processes (e.g., slow slip events, viscoelastic relaxation) which may delay or advance the next large event (e.g., Lin and Stein, 2004), spatiotemporal changes in interseismic plate locking (e.g., Chlieh et al., 2008; Prawirodirdjo et al., 2010), and/or upper plate deformation (Rosenau and Oncken, 2009). As monitoring techniques develop, evidences for time-variable slip at sub-seismic cycle scale emerge. The 2010 Chile earthquake case for example showed coseismic slip (as inferred from teleseismic inversion) which was predictable to first-order by assuming a time-

* Corresponding author.
E-mail address: marcos@gfz-potsdam.de (M. Moreno).

0012-821X/$ – see front matter © 2011 Elsevier B.V. All rights reserved.
doi:10.1016/j.epsl.2011.03.025

invariable locking pattern persistent over the preceding interseismic interval (Moreno et al., 2010). However, deformation models based on geodetic observations and including postseismic slip and upper plate deformation show less correlation between co, post- and preseismic slip patterns (e.g., Lorito et al., 2011). These new observations demonstrate that slip along the plate interface may vary to at least some degree either over the course of a single seismic cycle or from one cycle to the next cycle.

Here, we investigate the spatial and temporal variability of interseismic locking and its similarity with coseismic slip patterns along the South–Central Chile margin. This region hosted the southern termination of the 2010 (M_w=8.8) Maule earthquake and the rupture zone of the great 1960 (M_w=9.5) Valdivia earthquake (Fig. 1). As opposed to the zone of the 2010 Maule event which has been monitored preseismically, the megathrust in the study area has been monitored in its postseismic stage (with respect to the 1960 event) thus providing another key observation of the evolution during a seismic cycle. We use Finite Element models (FE-models) constrained by published and new GPS data spanning the period of time between 1994 and 2009 to simulate the earthquake cycle deformation half a century after the Valdivia earthquake and to derive a detailed image of the current locking degree. We discuss the inferred locking pattern with respect to its temporal variability and accumulated seismic potential to be released in future earthquakes.

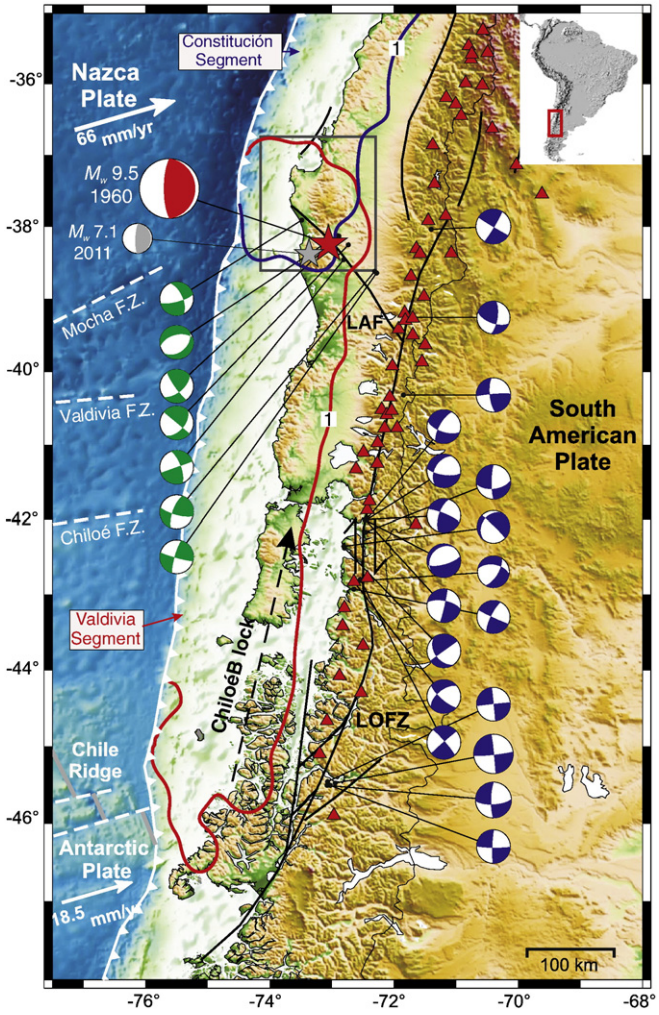

Fig. 1. Main tectonic features of the southern Andes. Blue and red lines define the rupture zones (>1 m) of the 1960 Valdivia (Moreno et al., 2009) and 2010 Maule (Tong et al., 2010) megathrust earthquakes, respectively. Fault plane solutions and epicenters of the 1960 (red) and the 2011 Mw 7.1 aftershock (gray) are shown. Square indicates the Arauco peninsula, where both earthquake segments overlap. Focal mechanisms of shallow crustal earthquakes below the surface trace of the Liquiñe-Ofqui fault zone (LOFZ) (blue) and Lanalhue Fault (LAF) (green) are also depicted (data compiled from Global Centroid-Moment-Tensor (CMT) catalog, Haberland et al. (2006) and Lange et al. (2008). Black lines denote major upper plate faults. Red triangles indicate active volcanoes. (For interpretation of the references to color in this figure legend, the reader is referred to the web version of this article.)

2. Seismotectonics of South–Central Chile

This margin has been the location of several large subduction earthquakes during the last few centuries, delineating two major adjacent seismotectonic segments: the Constitución and the Valdivia segments, affected by the 2010 Maule and 1960 Valdivia megathrust events, respectively (Fig. 1).

The 2010 Maule earthquake ruptured a segment of the Andean subduction zone, the Constitución segment, which was suspected of having a high seismic potential (seismic gap) on the basis of historic events (e.g., Campos et al., 2002) and supported by space-geodetic measurements (Moreno et al., 2008; Ruegg et al., 2009). Slip models (Lay et al., 2010; Tong et al., 2010), as well as coastal uplift data (Farías et al., 2010) suggest that the Maule earthquake rupture zone extended from 34°S to 38°S, affecting the entire Constitución segment. The patchwork of interseismic locking distribution derived by inversion of GPS observations during the previous decade (Madariaga et al., 2010; Moreno et al., 2010) indicated that the plate interface was generally highly but heterogeneously locked along the rupture area.

To the south, the Valdivia segment (between 37.5°S and 46°S) was in turn affected by the Great Chilean Earthquake of 1960, which is the largest seismic event recorded by modern seismology. This earthquake ruptured ~1000 km of the Nazca–South America plate boundary, with an average slip of 17 m and a local maximum of 44 m (Barrientos and Ward, 1990; Moreno et al., 2009). Contemporaneous surface deformation within the Valdivia segment includes the effects of protracted postseismic mantle rebound, in addition to locking of the seismogenic zone (Hu et al., 2004; Khazaradze et al., 2002). This interpretation arises from the fact that coastal GPS vectors within the 1960 rupture area are smaller than those to the north, and inland GPS sites (along the intra- and back-arc zones) move seaward, in the opposite direction to the interseismic contractional deformation. The 1960 rupture zone correlates also with the extent of the ~1000-km-long Liquiñe-Ofqui Fault Zone (LOFZ) (Cembrano et al., 1996; Rosenau et al., 2006). The forearc sector adjacent to the Liquiñe-Ofqui Fault Zone has been described as a northward translating sliver, the Chiloé block, decoupled from stable South America, as indicated by geological (Rosenau et al., 2006), seismological (Lange et al., 2008) and GPS data (Wang et al., 2007).

These two seismotectonic segments overlap in the Arauco peninsula area (Fig. 1), which is a major promontory along the Pacific margin of South America in terms of coastline morphology. It is a stable morphotectonic feature since the Pliocene and characterized by a high quaternary uplift rate (Melnick et al., 2009). The southern limit of this forearc segment coincides with the Lanalhue Fault (LAF), which is a crustal-scale fault inherited from Permian times (Glodny et al., 2008). Clusters of crustal seismicity (Haberland et al., 2006) as well as heterogeneous surface deformation (Moreno et al., 2008) indicate forearc fragmentation and heterogeneous stress distribution across this structure. An earthquake of magnitude M_w=7.1 occurred in January 2011 on this segment boundary (Fig. 1). It has been the largest aftershock yet related to the Maule earthquake.

The oceanic Nazca plate in South–Central Chile is characterized by the Valdivia Fracture Zone system at 40°S as the major tectonic feature (Fig. 1). This lithospheric discontinuity separates oceanic crust generated at the Chile Rise to the south, from crust that formed at the East Pacific Rise to the north (Tebbens and Cande, 1997). Both features may potentially influence co- and interseismic slip pattern.

3. GPS observations

Our GPS data set was collected at 42 survey mode (SGPS) GPS sites and 12 continuous (CGPS) stations. The SGPS data were observed on existing benchmarks during six regional surveys between 2002 and 2009 (Table 1), within the framework of the South American Geodynamic Activities (SAGA) project (Klotz et al., 2001). Additional key observations were also conducted at sites in the proximity of Concepción, and at trench-near islands both in the 2010 and 1960 segments. The CGPS stations were operated by the University of Concepción (MARI, MOCH, PCHE, and UDEC), Transportable Integrated Geodetic Observatory (BULS, CONZ, HUAL, and SAJU), University of Potsdam (GUAF and MELK), GFZ-Potsdam (PMO1) and Central Andes GPS Project (ANTC). To achieve a regional velocity field for the study area, we combined our GPS vectors with 86 published velocities (Klotz et al., 2001; Ruegg et al., 2009; Wang et al., 2007). The published vectors span the period between 1994 and 2005. The GPS data have been processed using the Bernese GPS Software Version 5.0. Processing models and strategies were adopted from the double-difference processing routine of Dach et al. (2007) and are explained in details in the Supplementary data.

The daily repeatabilities of the coordinates for subsequent epochs were ~2 mm in the horizontal components and ~6 mm for the vertical component. Time-series of horizontal coordinates derived

Table 1
Site positions and velocities, in ITFR 2005 and relative to South-America plate.

Site	Position (°)		Velocity/ITRF2005 (mm/yr)			Velocity/S.A. (mm/yr)		Uncertainties (mm/yr)			Time epochs (yr)
	Longitude	Latitude	Vlon	Vlat	Vup	Vlon	Vlat	σlon	σlat	σup	
SGPS											
AGUA	−73.342	−41.770	9.76	15.43	15.18	8.60	4.38	2.03	1.16	0.64	2005.87–2009.96
AREN	−72.662	−41.665	7.63	15.91	−2.79	6.57	4.78	2.33	0.52	1.06	2008.16–2009.96
AROA	−72.771	−36.736	29.53	20.40	−2.15	29.12	9.28	1.33	1.05	2.37	2002.53–2008.12
ATEM	−72.639	−38.769	12.56	21.54	6.43	11.89	10.41	0.98	0.73	1.02	2005.86–2008.12
CACH	−73.211	−36.772	34.86	20.89	1.90	34.40	9.82	2.10	3.08	8.64	2002.92–2009.96
CALF	−73.388	−39.754	17.67	22.44	8.67	16.78	11.39	3.20	0.50	2.06	2005.87–2009.92
CHOL	−72.442	−42.028	−0.25	12.99	5.27	−1.33	1.84	0.91	0.99	2.65	2005.87–2009.96
CLAS	−72.668	−39.285	11.25	15.07	5.85	10.51	3.94	0.39	0.85	1.20	2003.87–2005.86
FTRN	−72.377	−40.130	6.12	13.26	15.90	5.30	2.10	2.01	1.34	3.20	2005.87–2009.96
GUAB	−74.027	−41.806	21.64	18.60	−5.91	20.39	7.63	1.35	0.54	1.94	2005.87–2009.97
ICAL	−71.294	−38.825	1.83	5.71	−2.39	1.32	−5.57	0.69	0.78	2.15	2005.86–2008.12
IMOR	−73.664	−37.723	30.12	23.83	13.01	29.47	12.82	2.80	2.82	2.60	2003.88–2009.96
LAJA	−72.520	−37.256	26.90	15.38	3.50	26.45	4.24	0.84	0.74	3.70	2003.88–2008.13
LANA	−73.321	−37.930	21.86	18.94	10.80	21.23	7.89	2.38	2.00	2.50	2003.88–2009.96
LEBU	−73.668	−37.596	35.19	25.20	−20.08	34.56	14.19	2.19	1.43	2.10	2004.43–2007.03
LINC	−72.404	−40.623	−6.80	9.71	24.88	−7.69	−1.45	1.93	0.20	2.60	2005.87–2009.95
LLIC	−73.575	−37.192	40.93	22.54	−4.81	40.37	11.52	2.09	1.83	2.50	2002.93–2009.96
MADA	−73.721	−40.949	20.62	20.43	14.78	19.52	9.42	0.94	0.56	1.80	2005.87–2009.95
MANZ	−71.709	−38.468	6.81	9.50	6.98	6.30	−1.73	0.74	0.26	1.65	2005.86–2009.95
MARI	−74.286	−45.090	15.82	14.87	21.57	14.08	3.93	1.52	3.15	0.30	1994.11–2007.11
MULA	−71.346	−37.896	10.67	6.15	7.23	10.28	−5.12	1.14	0.87	2.70	2005.86–2009.96
NACI	−72.689	−37.607	21.19	16.75	8.13	20.67	5.62	2.75	1.40	6.04	2002.93–2009.96
NAHU	−73.031	−37.824	16.10	19.38	7.52	15.51	8.29	2.44	3.21	11.00	2003.88–2008.15
OSOR	−73.142	−40.590	11.99	15.33	23.21	11.02	4.26	1.23	1.60	2.53	2005.87–2009.96
PANG	−72.307	−39.679	6.89	14.20	11.75	6.14	3.03	1.77	0.20	3.06	2005.87–2009.93
PAST	−71.473	−39.584	3.36	8.27	9.05	2.73	−2.99	0.75	0.88	4.25	2005.86–2009.94
PEHO	−71.074	−38.597	7.22	7.43	9.23	6.77	−3.87	1.01	0.56	2.78	2005.86–2009.95
PSAA	−73.405	−38.778	25.06	19.10	8.67	24.30	8.06	2.16	1.33	2.61	2002.93–2009.96
PUAW	−72.393	−38.338	13.70	15.89	11.58	13.12	4.73	0.14	0.00	0.13	2005.86–2009.96
PUCA	−73.720	−40.547	22.86	19.66	6.33	21.82	8.65	1.35	0.77	2.23	2005.87–2009.94
PUCO	−71.990	−39.267	6.56	11.84	10.63	5.91	0.64	0.97	0.82	2.88	2005.85–2009.94
QUID	−73.491	−38.242	24.42	19.29	−2.26	23.72	8.26	1.74	1.26	2.33	2002.93–2009.96
RALU	−72.312	−41.379	2.18	12.29	8.28	1.20	1.12	1.83	0.99	2.24	2005.87–2009.95
SFAB	−71.321	−36.663	19.44	14.21	2.22	19.21	2.93	0.78	0.87	1.75	2002.93–2008.13
STCA	−73.530	−37.059	41.01	23.03	−5.19	40.47	12.00	2.30	0.79	2.60	2004.32–2009.20
STCL	−72.361	−36.836	28.47	16.05	7.62	28.10	4.89	1.47	1.38	7.86	2002.93–2009.96
STDO	−73.546	−37.023	40.94	22.98	−8.85	40.40	11.95	2.08	1.31	2.51	2004.32–2009.20
STJU	−72.849	−37.206	28.12	19.01	5.48	27.64	7.90	0.21	0.00	0.74	2003.87–2008.13
TIRU	−73.502	−38.341	21.68	20.99	36.86	20.96	9.96	2.50	0.74	24.00	2003.89–2007.05
TMOL	−71.711	−38.966	8.18	8.62	10.52	7.60	−2.61	1.08	0.89	1.67	2005.86–2009.96
TOLT	−73.182	−39.349	16.32	18.60	10.93	15.51	7.53	0.69	0.30	2.40	2003.87–2005.86
VARA	−73.238	−38.531	18.65	20.99	9.65	17.94	9.93	0.58	0.15	1.01	2003.88–2008.15
CGPS											
ANTC	−71.532	−37.338	16.27	10.47	0.25	15.93	−0.78	0.01	0.10	0.02	2005.03–2009.16
BULS	−72.295	−36.741	26.91	19.56	11.24	26.56	8.39	2.86	1.43	2.22	2009.10–2010.10
CONZ	−73.026	−36.844	32.66	20.12	1.15	32.21	9.03	1.01	1.71	1.57	2007.18–2009.41
GUAF	−74.827	−43.566	45.92	21.10	−34.30	44.32	10.22	0.44	0.55	2.90	2009.14–2010.15
HUAL	−73.190	−36.746	34.45	21.86	−2.51	33.99	10.79	1.37	0.89	3.37	2005.85–2008.31
MELK	−73.749	−43.897	8.25	14.18	2.28	6.75	3.18	1.86	1.93	3.56	2009.21–2010.15
MOCH	−73.900	−38.400	33.87	18.59	−1.07	33.10	7.60	1.34	2.05	1.95	2002.69–2010.15
MRQT	−72.444	−42.031	−0.60	4.62	5.10	−1.68	−6.53	0.20	0.30	0.30	2008.20–2009.40
PCHE	−72.649	−41.741	−1.30	9.30	8.60	−2.37	−1.83	0.10	0.20	0.20	2008.20–2009.40
PMO1	−72.939	−41.469	1.38	12.72	2.31	0.31	1.62	0.10	0.17	0.01	2007.90–2009.33
SAJU	−72.931	−37.175	32.82	20.43	17.09	32.33	9.33	2.17	1.32	2.11	2009.02–2010.10
UDEC	−72.340	−37.472	22.12	17.79	−1.27	21.66	6.63	0.04	0.11	0.02	2005.06–2008.99

from SGPS showed an approximately linear behavior during the observation period. Only the LLIC, LEBU and IMOR coastal sites experienced minor non-linear motions. Horizontal components of CGPS stations also fit well into a linear trend (Figure S1). Although horizontal station coordinates show linear trends, we cannot rule out the possible occurrence of local transient slip events given the low frequency of SGPS observations and the sparse distribution of CGPS sites. Moreover, differences on magnitude and direction between published and new velocities of common sites may be related to transient deformation over different time windows (Table 1).

Both the new and the previously published GPS vectors show regional-scale heterogeneity pointing to deformation partitioning within the study area (Fig. 2). Four features of the velocity field are observed. Firstly, GPS vectors in the Constitución segment (measured before the 2010 event) are parallel to the direction of plate convergence and their magnitudes decrease progressively inland. Coastal site velocities in this segment reach over 40 mm/yr. Secondly, GPS vectors in the Valdivia segment have lower magnitudes than those to the north, and back-arc vectors move seaward. Thirdly, a regional-scale clockwise rotation is broadly distributed in the arc and back-arc, across the earthquake segment boundary, where coastal GPS vectors also vary markedly in both orientation and magnitude, and fourthly, published GPS vectors south of 42 °S show high northward displacements, a feature that is not clearly shown by our new observations.

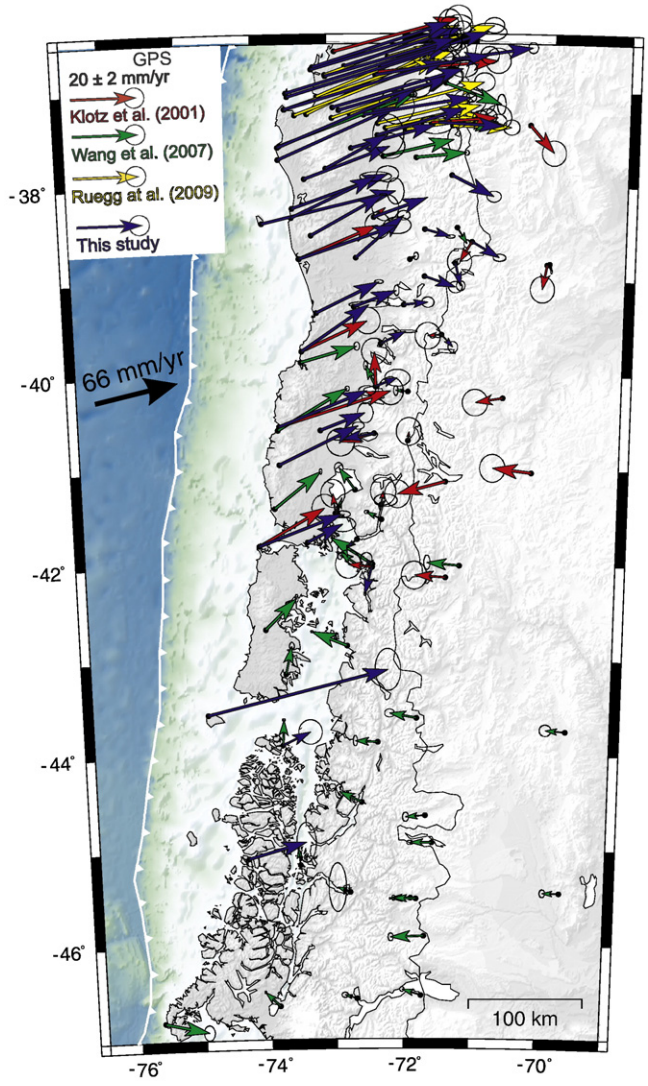

Fig. 2. GPS vectors in the southern Andes relative to a stable South American reference frame. GPS velocities derived in this study are shown with blue arrows (Table 1). Published vectors from Klotz et al. (2001), Wang et al. (2007), and Ruegg et al. (2009) are depicted by red, green, and yellow arrows, respectively. Ellipses represent 95% confidence limits. (For interpretation of the references to color in this figure legend, the reader is referred to the web version of this article.)

4. Kinematic finite element modeling

Deformation models were performed using the Finite Element Method (FEM). The surface deformation was predicted kinematically from fault-slip, regardless of the loading mechanism and frictional properties. Fault-slip was modeled using the split-node technique (Melosh and Raefsky, 1981) applying linear constraint equations. Our spherical FE-models incorporate topography and bathymetry data, as well as the geometry of the subduction slab and the continental Moho derived from recent geophysical transects (Contreras-Reyes et al., 2008, 2010; Haberland et al., 2006, 2009; Lange et al., 2008; Tassara et al., 2006) (Fig. 3). Details related to the modeling configuration are described in the Supplementary data.

4.1. Modeling strategy

Velocities in the direction of plate motion are readily explained by elastic deformation caused by a locked or partially locked plate interface (Savage, 1983). Trenchward velocities, however, cannot result from a model in which a locked (or freely slipping) shallow interface is the only mechanism causing deformation. The observed trenchward motion has been suggested to be a consequence of postseismic viscoelastic deformation following the 1960 earthquake. Because the interseismic locking pattern, which is the primary target of our study, is masked by this postseismic relaxation pattern, modeling postseismic scenarios is a major issue here. Thus, we had to derive first the postseismic signal at the time of the GPS observations before inferring the locking distribution. In doing so, our modeling consisted of four steps, which are summarized below and explained in greater detail in Sections 4.2–4.4.

(1) Simulation of a postseismic viscoelastic velocity field 45 yr after the 1960 earthquake, derived by introducing a coseismic slip pattern, derived using the same model configuration (Moreno et al., 2009), into a viscoelastic model. In this step, different scenarios of postseismic response are calculated for a wide range of constant values of continental mantle viscosity.
(2) Estimation of the locking rate distribution for different mantle viscosity values. Here, we corrected the GPS vectors for the postseismic signals that resulted from each viscosity value of step 1 and then inverted for the locking rate using FEM-generated Green's functions.
(3) Analysis of sensitivity to lateral variation of mantle viscosity structure. For that, we divided the margin in six segments, and assumed different values of continental mantle viscosity. For each viscosity value, the total deformation field, which resulted from the combination of interseismic and postseismic, is then compared with the GPS velocities. This comparison allowed the estimation of an optimal viscosity structure and the best fitting postseismic velocity field.
(4) Derivation of the degree of interseismic locking along the plate interface. Here, the preferred postseismic signal was subtracted from the GPS vectors and the corrected velocities inverted for the locking degree.

4.2. Postseismic viscoelastic velocity field

The system's response to the earthquake was modeled by prescribing an instantaneous coseismic slip as initial condition for stress perturbation in the upper mantle. In doing so, we introduced the coseismic slip distribution derived by Moreno et al. (2009) employing

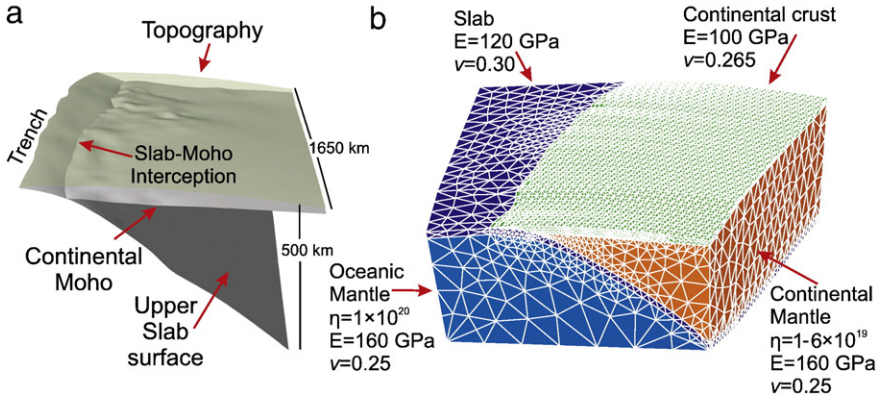

Fig. 3. 3-D model configuration. a) FE-models include topography and bathymetry, as well as a precise geometry of the slab and continental Moho, which were derived from combining available geophysical information. b) The model structure consists of an elastic upper plate, an elastic subducting plate, a viscoelastic continental mantle, and a viscoelastic oceanic mantle.

the same FE-model configuration as this study. The coseismic slip distribution was introduced into the nodes of the fault and an instantaneous load step computed. The nodes on the interface were subsequently set free from constraints (no slip), and 20 substeps computed for an equivalent time period of 45 yr (averaged time of the GPS observations). A generalized Maxwell solid rheology model was used to represent the viscoelastic response. This viscoelastic rheology is appropriated to simulate postseismic velocities decades after an earthquake (e.g., Hu et al., 2004; Suito and Freymueller, 2009).

Given that the model geometry and the coseismic slip model were fixed, the main adjustable parameter in the postseismic viscoelastic model was the upper mantle viscosity (η). Inland horizontal velocities due to stress relaxation strongly depend on the viscosity of the continental mantle and they are little influenced by the oceanic mantle viscosity (Hu et al., 2004). The oceanic mantle viscosity was fixed in the models to 1×10^{20} Pa s following the finding of Hu et al. (2004), in which this value better reproduces the vertical deformation. We computed postseismic viscoelastic response for a broad range of homogeneous continental mantle viscosities (from 1×10^{19} Pa s to 6×10^{19} Pa s), which are equivalent to Maxwell relaxation times ($T=\eta/\mu$: μ is the rigidity, assumed to be 64 GPa) of 5 yr to 30 yr. This modeling step considering a variety of homogeneous viscosity structures served as a guide for end member scenarios (from low to high viscosity) for postseismic relaxation velocities.

4.3. Locking rate distribution for homogeneous viscosity structures

Horizontal components of GPS vectors were corrected for the postseismic viscoelastic signals derived from each viscosity scenario. Then each corrected velocity data set was used to infer a locking rate distribution corresponding to each viscosity value. Interseismic deformation has been numerically simulated using the back-slip modeling approach (Savage, 1983), which involves dislocations of coupled areas, rather than actual forward slip on surrounding regions. We estimated back-slip displacements (dip-slip and strike-slip) along a curved fault by using an inversion method based on FEM-generated Green's functions, following the technique of Masterlark (2003). Isoparametric finite elements with quadratic shape functions were implemented to constrain the slip distribution (Laplacian matrix) of nodes in a heterogeneous grid (Moreno et al., 2009). The Laplacian matrix ensures that the differences in slip between a node and its direct neighbors are small, resulting in a stable solution. The smoothing parameter that controls the Laplacian operator, β, was estimated from the trade-off curve between misfit and slip roughness (e.g., Bürgmann et al., 2005).

We introduced a convergence rate of 66 mm/yr (Angermann et al., 1999; Kendrick et al., 2003) for the Nazca plate. The 3-D back-slip directions along the strike of the margin were estimated from the angular vector of the Nazca plate, and were introduced through the use of a local coordinate system for each fault node. Minimum and maximum slip constraints were applied to avoid models with unrealistic slip patterns and to improve the model's resolution (Du et al., 1992; Harris and Segall, 1987). The back-slip rate was constrained to a range between 0 and 66 mm/yr, representing slip at plate convergence rate, and fully locked areas, respectively. The locking degree was calculated by dividing the estimated back-slip rate by the plate convergence rate. Thus, the degree of locking ranged from 0, for areas where plate convergence was accommodated by full slip, to 1, for non-slipping areas, i.e. fully locked.

We selected in the inversion only fault nodes localized above a depth of 60 km, assuming the down-dip limit of the locked zone to be not deeper along the southern Andes, as suggested by previous geodetic studies (Moreno et al., 2008; Ruegg et al., 2009; Tong et al., 2010; Wang et al., 2007). This resulted in the selection of 401 node-pairs. Below the down-dip edge of the fault plane we constrained the back-slip to zero, i.e. assuming aseismic slip at plate convergence rate at depth. A similar constraint was introduced on the nodes along the trench to simulate an upper aseismic zone (Oleskevich et al., 1999). By introducing an aseismic updip transition, inland deformation was not affected and velocities of coastal sites were better reproduced.

In order to examine the resolving power of the GPS network and our inversion method we carried out a checkerboard resolution test. In doing so, the fault plane was discretized into regular alternating patches, with either 0 or 1 degree of locking. The velocities at the GPS sites were estimated using a forward model that introduces the checkerboard patterns as fault-slip conditions. The uncertainties of GPS velocities were added to compile a set of synthetic data, which was subsequently inverted to obtain the distribution of the degree of locking. According to this analysis, our inversion is capable in recovering the main features of synthetic checkerboard patches over most of the region (Figure S2). Fault-slip resolution was poorest offshore and improved in the down-dip direction. Better resolution was achieved north of 39°S, where the GPS network extended to islands near the trench and had a higher spatial density.

4.4. Optimal upper mantle viscosity and postseismic–interseismic velocity field

To explore the influence of lateral variations of the viscosity structure on the observed velocity field, we performed a sensitivity test, in which the interseismic deformation was fixed and the viscosity value was derived. In carrying out this test we divided the margin into six latitudinal segments of two-degree length (from 48°S to 36°S) and computed the total deformation field for a selected range of viscosity values (from 2×10^{19} Pa s to 5×10^{19} Pa s). Within each segment we minimized the root-mean-square (RMS) difference between the total

surface displacements (interseismic plus postseismic models) and the GPS velocities. By using the preferred viscosity structure, the best fitting postseismic viscoelastic velocity field was estimated. The optimal postseismic velocities were then subtracted from the GPS vectors and a preferred locking rate distribution was computed.

5. Results

5.1. Postseismic viscoelastic deformation field

The predicted viscous relaxation significantly varies as function of the assumed viscosity structure, which controls the relaxation time and the surface deformation magnitude (Fig. 4 and Figure S3). Our viscoelastic models predicted significant displacements 50 yr after the earthquake. Postseismic trenchward velocities extend over the entire length of the 1960 earthquake rupture zone, confirming the findings of Hu et al. (2004). Significant deformation does not extend far beyond the rupture zone in the along-strike direction, but significant viscoelastic deformation does extend for several hundred kilometers inland from the coseismic rupture zone decreasing toward the trench. Clearly, the pattern of mantle flow and the resulting surface displacements were highly sensitive to the coseismic slip distribution. Maximum postseismic viscoelastic motion is found landward of the down-dip end of the central area of the 1960 rupture where highest coseismic slip was released (39°S–42°S). A broadly-distributed counterclockwise rotation results from the postseismic response at the northern edge of the earthquake rupture zone (Figure S3).

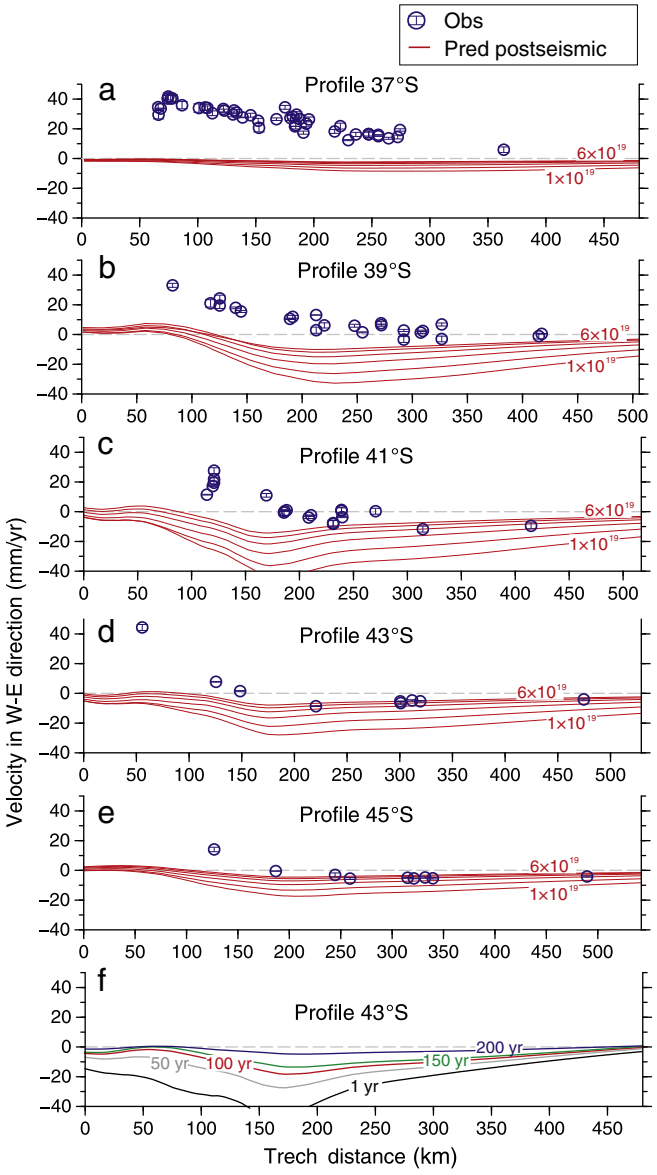

Fig. 4. Surface velocities in response to the viscoelastic relaxation along W–E profiles. a–e) Computed postseismic viscoelastic velocities for different values of mantle viscosity, which ranges from 1×10^{19} to 6×10^{19} Pa s (red lines). GPS velocities are shown by blue circles. Models that introduced viscosity values of 2×10^{19} Pa s, 3×10^{19} Pa s, 4×10^{19} Pa s and 5×10^{19} Pa s (models A, B, C and D) produced a reasonable postseismic response that may explain the observed trenchward displacements. f) Predicted postseismic surface velocities using a viscosity of 3×10^{19} Pa s (Model B) for different time windows, which range from 1 yr to 200 yr after the earthquake. (For interpretation of the references to color in this figure legend, the reader is referred to the web version of this article.)

Models with lower viscosity (1×10^{19} Pa s) produced an excess of surface motion both in the near and far-field (Fig. 4a–e). Conversely, models with higher viscosity values (6×10^{19} Pa s) led to poor velocity response along the back-arc. In general, models loaded with viscosity values of 2×10^{19} Pa s, 3×10^{19} Pa s, 4×10^{19} Pa s and 5×10^{19} Pa s (hereafter referred to as models A, B, C and D, Fig. 4 and Figure S3) produced a reasonable range of surface displacements that can be used to explain the trenchward component of motion observed in the present velocity field (Fig. 2), and they can be considered as a priori candidate scenarios to simulate viscous relaxation. These values are consistent with those previously inferred for this area on the basis of modeling the earthquake-cycle (Hu et al., 2004; Khazaradze et al., 2002).

Fig. 4f shows predicted surface motion in the W–E direction at different times based on model B. The postseismic response was very pronounced in magnitude 1 yr after the earthquake and decreased with time as the stress was released. The predicted velocities were up to 10 mm/yr 150 yr after the event and significantly declined after 200 yr.

5.2. Locking rate distribution for different viscosity structure scenarios

Inversion results from the best fitting model of each corrected data set (Figure S4) are show in Fig. 5. The interseismic velocity fields based on models A and B were not capable of reproducing the corrected vectors in the north–central part of the rupture, but these models provided a good fit to the far-field velocities south of 43°S (Fig. 5 and Figure S5). Models A and B produced a RMS of 7.63 mm/yr and 5.04 mm/yr, respectively. Models based on higher viscosity, C and D, significantly improved the model fit of the north–central area and reduced the RMS to 4.56 mm/yr and 4.8 mm/yr, respectively. However, postseismic response of Model D is poor as shown by trenchward residual velocities along the back-arc (Fig. 5d).

While varying in detail, the different locking inversions based on different postseismic scenarios lead to a similar first-order pattern (Fig. 5) with some common features. The inversion results confirm that north of 38°S, the area that corresponds to the southern termination of the rupture zone of the 2010 Maule earthquake, the plate interface was highly locked before the earthquake. Additionally, inversion results suggest that the central area of the 1960 rupture zone, where the highest coseismic slip occurred (>40 m), is fully coupled at present accumulating significant amounts of interseismic strain. South of 43°S, the interface appears to be less locked, with locking localized in two patches. Interestingly, locked patches in the south coincide with islands representing emerged sectors of the continental shelf, however in these areas the resolution was generally poor. At the northern limit of the 1960 Valdivia earthquake segment (39°S–38°S), a wide, less locked area is found reflected by low margin-normal velocities observed on coastal sites.

5.3. Upper mantle viscosity and optimal postseismic velocity field

The wide range of viscosity values fitting the data to first-order but differently in detail suggest an irregular viscosity structure (Fig. 5 and

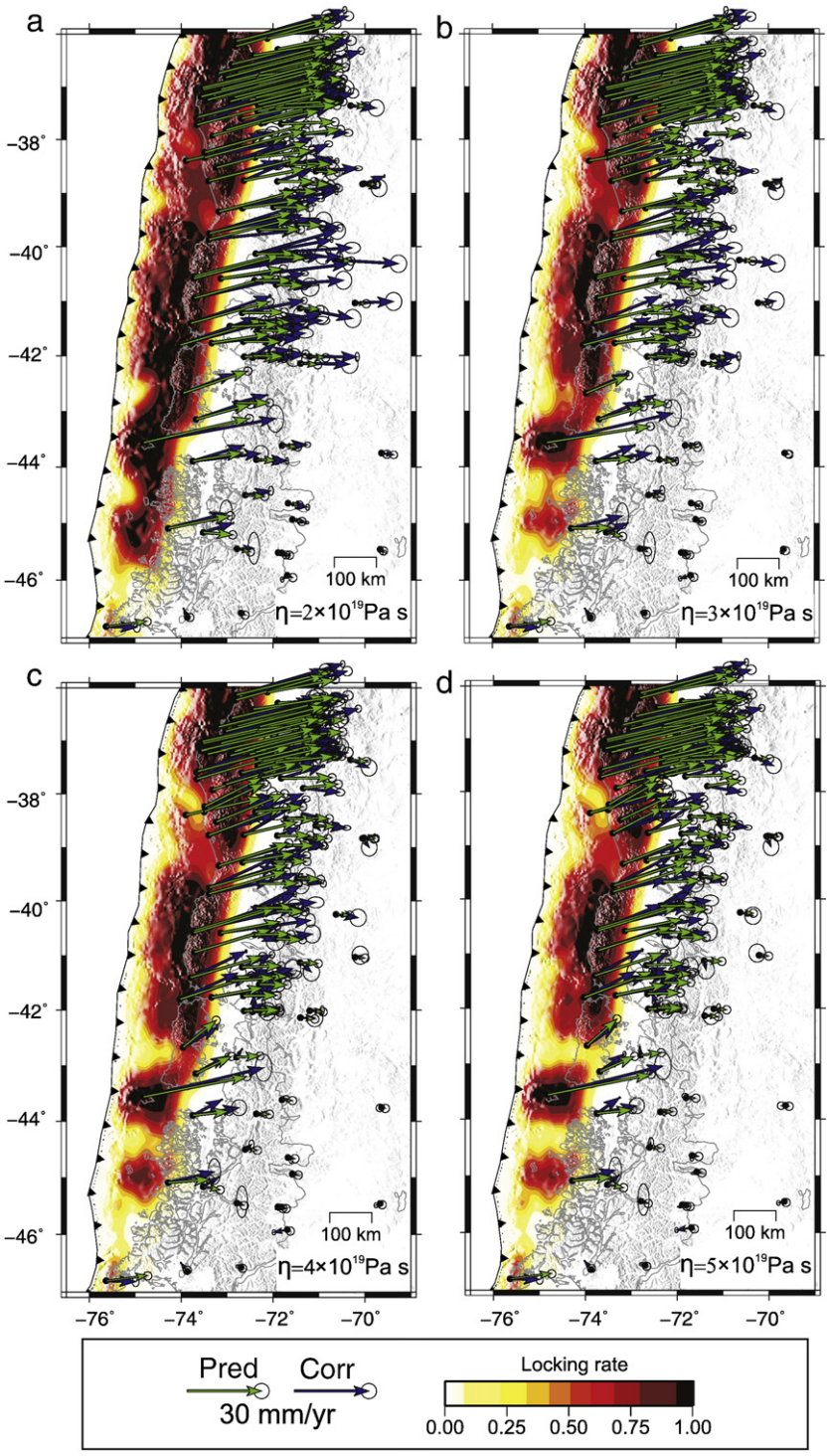

Fig. 5. Locking distributions for different scenarios of uniform mantle viscosity. a–d) Locking distribution based on models A, B, C and D, respectively. Predicted interseismic velocities and GPS vectors corrected by the postseismic signals are shown by green and blue arrows, respectively. Viscosity (η) increases from 2×10^{19} (a) to 5×10^{19}(d). (For interpretation of the references to color in this figure legend, the reader is referred to the web version of this article.)

Figure S5): a homogeneous distribution that fits the observations in the southern area produced an excess of viscoelastic response in the north–central (total deformation based on models A and B). Vice versa, a homogeneous distribution that fits the observations in the north–central area produces a deficit of viscoelastic response in the southern area (total deformation based on models C and D).

To explore the lateral variation of viscosity, we first fixed the interseismic velocity field that resulted from a model with a uniform, fully locked zone, in which the down-dip limit was based on the southward narrowing proposed by Wang et al. (2007).Then, we computed the total deformation for seven values of viscosity that ranged from 2×10^{19} Pa s to 5×10^{19} Pa s and estimated the RMS for six latitudinal segments (Fig. 6). The same procedure was done using the interseismic velocity results from best-fitting inversions based on models B and C, which provided a good fit in the southern and northern areas, respectively. We found that the total deformation based on the uniform locked zone as well as on models B and C produced similar RMS distribution in these segments. Results

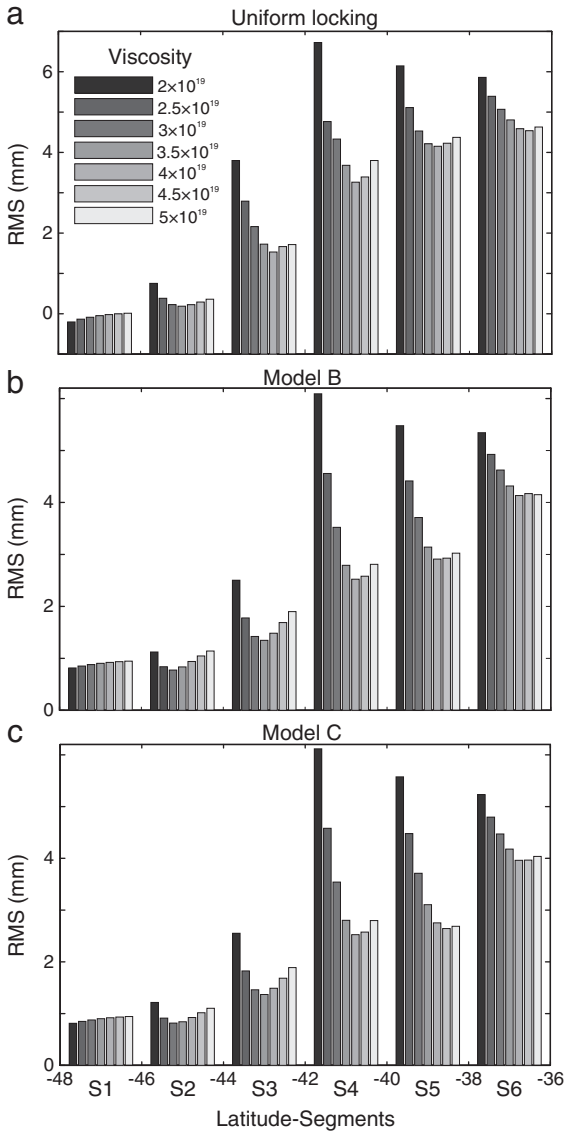

Fig. 6. Sensitivity test to explore lateral variations on upper mantle viscosity using fix interseismic velocity fields. The margin was divided into six latitudinal segments of two-degree length (S1 to S6) and computed the root-mean-square (RMS) difference between the total surface displacements and GPS vectors for seven viscosity values (from 2×10^{19} to 5×10^{19} Pa s). a) Distribution of RMS that resulted by using the interseismic deformation based on a homogeneous locking distribution. b) Distribution of RMS that resulted by using the interseismic deformation based on model B. c) RMS distribution that resulted by using the interseismic deformation based on model C.

indicated that lateral variations on the viscosity structure lead to surface velocities more consistent with the GPS observations. The best fitting model came from a set in which the viscosity decreases southward, with values of 4×10^{19} Pa s to the north of 42°S, 3.5×10^{19} Pa s between 42°S and 44°S, and 3×10^{19} Pa s to the south of 44°S. In the segment between 46°S and 48°S, variation on viscosity structure induces changes of magnitude below the precision of the observations. Geodynamically, the southward decrease in viscosity is compatible with the increase in heat-flow that results from southward younging of the oceanic plate towards the Chile Rise (Fig. 1).

5.4. Locking rate distribution for optimal viscosity structure

The distribution of locking degree based on the velocities corrected from the optimal postseismic signal is shown in Fig. 7. This locking distribution shared first-order similarities with those that resulted from using the postseismic velocities of models B and C (Fig. 5). This model slightly improved the average fit to the observations (RMS = 4.2), but better reproduced the lateral variations of sites along the back-arc (see Supplementary data for error propagation). The preferred model suggests that the interseismic locking in the megathrust is heterogenous. The plate boundary is therefore accumulating slip deficit at spatially variable rates. The plate interface below the Arauco peninsula appeared to have been fully locked. In this region, the interseismic deformation is broadly distributed across the back-arc, producing about 15 mm/yr of eastward displacements at a distance of 300 km from the trench. The segment that ruptured in 1960 appears to be only partially locked and experiences significant aseismic slip. In this segment, inland interseismic deformation decreases with the southward narrowing of the coupling zone. Highly locked patches coincide with zones of substantial coseismic slip (over 20 m) (Fig. 8). However, not all patches of high coseismic slip have

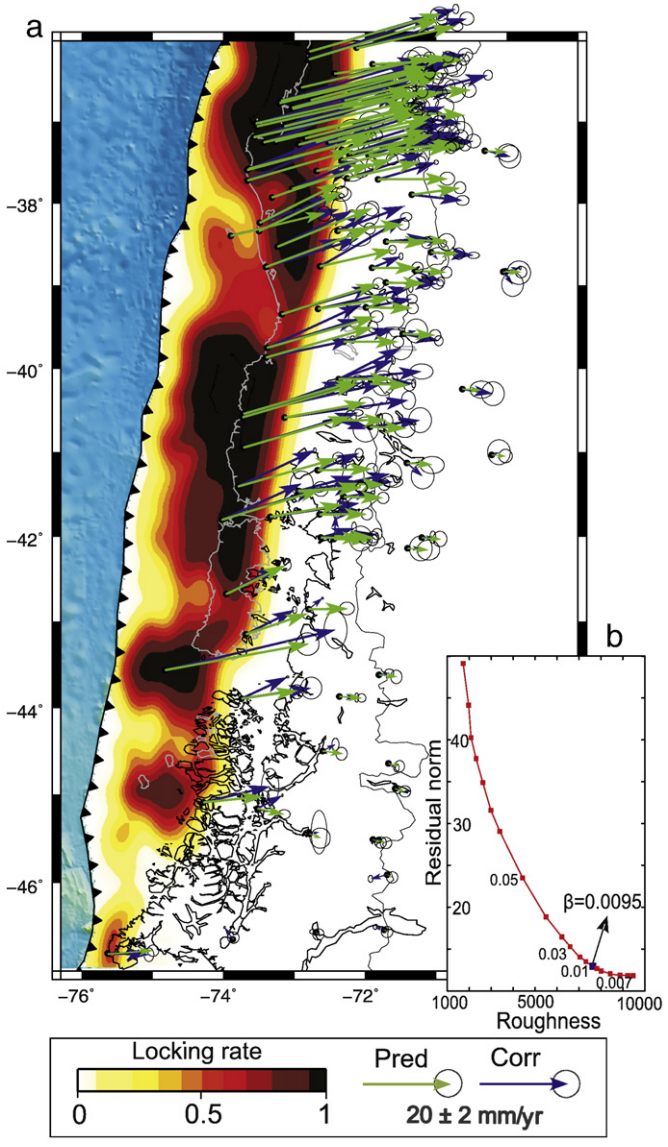

Fig. 7. a) Optimal distribution of locking rate in the plate interface. Predicted interseismic velocities and GPS vectors corrected by the postseismic signals are shown by green and blue arrows, respectively. b) Tradeoff curve for a broad range of the smoothing parameter (β). The optimal value for β is 0.0095 located at the inflection of the curve. (For interpretation of the references to color in this figure legend, the reader is referred to the web version of this article.)

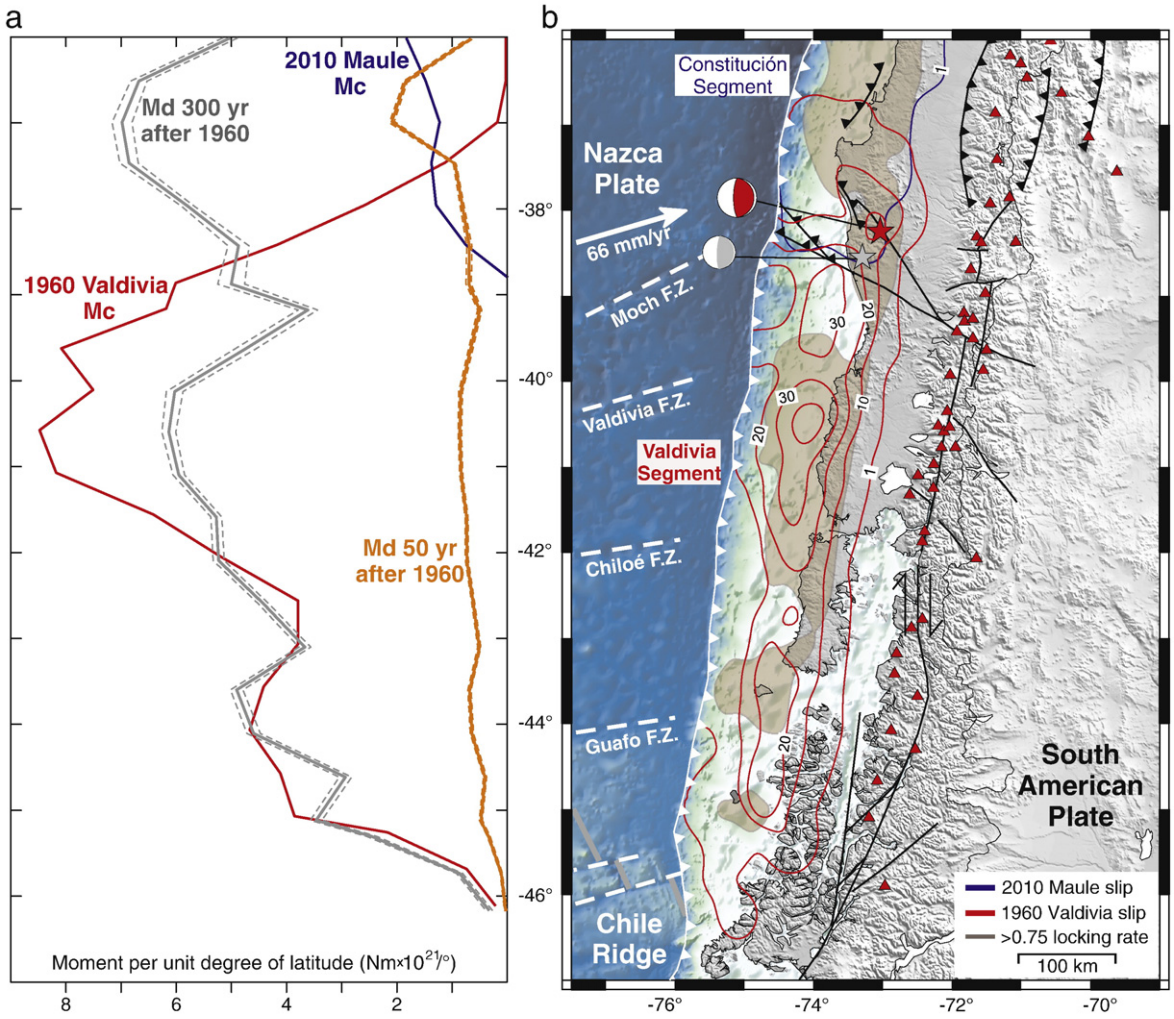

Fig. 8. a) Latitudinal distribution of the coseismic moment (Mc) released by the 1960 Valdivia (Moreno et al., 2009) (red line) and 2010 Maule (Tong et al., 2010) (blue line) earthquakes, and of accumulated deficit of moment (Md) due to interseismic locking of the plate interface 50 (orange line) and 300 (gray line) years after the 1960 earthquake, respectively. The range of errors of the Md rate is depicted by dashed lines. High rate of Md was found in the earthquake rupture boundary, where slip deficit accumulated since 1835 seems to be not completely released by the 2010 Maule earthquake. b) Schematic map showing the deformation processes that control the observed deformation in the southern Andes and the similarity between coseismic and locking patches. Blue and red contours denote the coseismic slip for the 2010 Maule (Tong et al., 2010) and 1960 Valdivia (Moreno et al., 2009) earthquakes, respectively. Patches with locking degree over 0.75 are shown by brown shaded areas. The 1960 earthquake (red star) nucleated in the segment boundary, area that appears to be highly locked at present. The 2011 Mw 7.1 aftershock (gray) may indicate that stress has been transmitted to the southern limit of the Arauco peninsula. (For interpretation of the references to color in this figure legend, the reader is referred to the web version of this article.)

been fully locked in the observation period, as shown by a low locking area at the northern edge of the Valdivia segment.

6. Limitations of the modeling approach

Though the present deformation field in the region affected by the 1960 earthquake is well observed, studying deformation components related to this event (e.g. ongoing postseismic response) represents a difficult issue because the available geodetic data leave some freedom. Uncertainties related to the coseismic slip distribution directly affect the postseismic viscoelastic response, and consequently the estimated degree of locking. As the focus of this study was to explore lateral variations of the postseimic viscoelastic deformation to infer the plate locking, we used the spatially-variable coseismic slip derived by Moreno et al. (2009), in which a well defined slab geometry (identical to this study) was used to invert the available geodetic data (Plafker and Savage, 1970). This coseismic slip fits well the observations and provides detailed information about the rupture distribution. Unfortunately, the geodetic observations used in this study include variable time intervals with respect to the earthquake and thus may be affected by early postseismic transient signals. However, (Plafker and Savage, 1970) reported that vertical displacements obtained shortly after the earthquake (Alvarez and Saint-Amand, 1963) were reasonably consistent with their observations, and therefore these geodetic data can represent a first-order estimate of coseismic displacements. Additionally, a joint inversion of tsunami and geodetic data (Satake and Fujii, 2010) hints at spatially heterogeneous coseismic slip similar in slip magnitude and distribution of asperities with the model introduced in this study.

The use of a different coseismic slip model leads to a different predicted postseismic signal (Figure S6). Hence, our postseismic and interseismic-modeled velocities are not unique and depend on the introduced coseismic slip. The zone of low coupling in the northern boundary of the 1960 rupture coincides with a patch that released high coseismic slip during this event, and therefore is unexpected. To test the robustness of this feature, we varied the coseismic slip in this area. In doing so, we computed the postseismic viscoelastic relaxation and the locking distribution for a coseismic slip set to 0.5 and 1.5 times the slip derived by Moreno et al., 2009 (Figure S6). In these simulations we used a homogeneous mantle viscosity of 3×10^{19} Pa s and 4×10^{19} Pa s. Results clearly indicated that the magnitude of the coseismic slip controls the postseismic response, and consequently induces to

different values of viscosity to fit the observations. Nevertheless, a reduced locking rate in this region is a common feature of these models. This indicates that the low locked zone is a robust feature needed to fit the velocities of coastal sites, which are poorly affected by the postseismic viscous relaxation (Figure S3 and Figure S6).

7. Discussion

7.1. Relationship to 1960 earthquake and time-variability

The proposed degree of locking revealed differences in the distribution of strain accumulation along the South-Central Chile margin over the past decade. Part of the plate interface that was highly locked corresponded to the southern part of the rupture area of the 2010 Maule earthquake. This segment was not completely ruptured by any M>8.5 earthquake since 1835, and consequently it was undergoing an advanced interseismic phase, as has been previously proposed (Campos et al., 2002; Ruegg et al., 2009).

In an attempt to quantitatively analyze the similarity of the interseismic and coseismic slip patterns and to assess the seismic potential of the region, we derived the coseismic moment (Mc) released by the Valdivia and Maule earthquakes, and the interseismic moment deficit rate (Md) for different time periods (Fig. 8a). The Mc released by the 1960 earthquake was highly non-uniform, with most of the moment being released in the north–central part of the rupture, which consisted of two adjacent asperities with slip over 30 m. However, given that only limited geodetic data are available for the 1960 earthquake, we cannot discard that those high-slip areas (>40 m) resulted from processes such as splay faulting, afterslip, or overestimated coastal subsidence due to sediment compaction. One of these asperities appears to be highly locked again. It may thus behave as a persistent asperity over at least two seismic cycles (Fig. 8). Based on the present Md which considers the theoretically accumulated slip deficit after the 2010 and 1960 earthquakes, a near future failure of this asperity may result in an earthquake of magnitude up to M~8 similar to the 1737 or 1837 events that affected this region (Cisternas et al., 2005). The probability for such an event to occur has presumably been increased due to stress transfer from the 2010 Maule earthquake. The aftershock of magnitude Mw = 7.1 that nucleated in the segment boundary may indicate that stress has been transmitted to the southern limit of the Arauco peninsula.

The average interval between giant earthquakes, such as the 1960 event, on this fault spans nearly 300 yr (Cisternas et al., 2005). However, the calculated Md at this interval does not balance the Mc related to the 1960 earthquake. This deficit is mainly because the area around 39°S, which showed high slip during the 1960 event, appears to be creeping today and may thus have not accumulated much slip since 1960. A way to reconcile the 1960 Mc is that this part of the fault re-locks in the future and/or strain accumulates over a longer period spanning more than one cycle. Such a time-variable locking pattern may also explain why some earthquakes are time-predictable (e.g., Shimazaki and Nakata, 1980) whereas others are not (e.g., Murray and Segall, 2002). Alternatively, it may also suggest that some asperities in the Valdivia segment are not persistent over multiple events in case the slipping area does not re-lock and fail again.

7.2. Relationship to seismotectonic segmentation and tectonic features

The seismotectonic segmentation of the margin is characterized by a first-order, long-lived (since Paleozoic) tectonic boundary at ~38°S defined seismically (historical earthquake record), morphologically (Arauco peninsula), structurally (Arauco Orocline, Lanalhue fault, end of Liquiñe–Ofqui Fault Zone) and petrographically (Eastern–Western Series contact) (e.g., Glodny et al., 2005, 2008; Melnick et al., 2009; Rehak et al., 2007). The segment boundary seems to accumulate large Md (Fig. 8a). At this latitude, the locking degree (onshore) is spatially uniform but coseismic slip from the 2010 and 1960 earthquakes tapers from north and south, overlapping at the center of the Arauco Peninsula. The resulting slip deficit in this region may be released postseismically (afterslip) or remain over an extended period of time. Alternatively, plate convergence may be accommodated at this latitude to a significant fraction by permanent upper plate shortening. This is supported by the presence of the Arauco peninsula as a unique coastal feature in South–Central Chile and associated active reverse faulting as well as high quaternary uplift rates (Melnick et al., 2006, 2009). If so, upper plate shortening may be considered as a relaxation barrier mechanism similar to creeping zones along the megathrust. Accordingly, significant slip deficit build-up is inhibited because convergence-induced stresses drive upper plate faults. However, to be a persistent feature over the interseismic period these upper plate faults would have to be weaker than the megathrust to ensure their activation in favor of megathrust failure.

A low locking zone south of the segment boundary coincides both with a coastline retreat and with a topography low with lower long-term uplift rates (Rehak et al., 2007), suggesting that the weak locking is likely a persistent feature expressed in the long-term deformation in this region. This area of aseismic slip correlates with a triangular block defined by the subduction of the Valdivia and Mocha Fracture Zones (Fig. 8). In the southern part, the subduction of the Chiloé and Guafo Fracture Zones also coincides with lateral variations of coupling. Hence, the incoming fracture zones may enhance the flux of chemically bound water into the subduction zone (Contreras-Reyes et al., 2008) and also influence the thermal regime inducing variations in the stick-slip like frictional behavior on the interplate. Similar correlations between low locking areas and the subduction of oceanic ridges or fracture zones have been shown in other regions (Chlieh et al., 2008; Konca et al., 2008; Perfettini et al., 2010), respectively. However, counter-examples (fractures zones which are coincident with high coupling) in those studies also indicate that low locking is not always correlated with the subduction of high oceanic features.

8. Conclusions

We studied the spatial and temporal variability of plate locking in the South–Central Chile subduction zone. Based on surface velocities measured by GPS and on FEM inversion techniques, we inferred the decadal-scale locking pattern. Accordingly, the southern termination of the rupture zone of the 2010 Maule earthquake appeared to be fully locked in the decade preceding the event. In contrast, a significant amount of creep occurred along the Valdivia segment, which last ruptured in 1960. The interface here is fully locked in the central part of the 1960 rupture zone, where highly-locked patches coincide with high-slip regions of the 1960 earthquake. These patches have already the potential for a M~8 earthquake and may be triggered to fail by static stress changes from the 2010 Maule earthquake.

Extrapolated to the ~300-yr recurrence period of giant earthquakes in the area, the hypothetically accumulated moment deficit does not balance the complete coseismic moment of a Valdivia type earthquake. This may indicate that either the locking distribution has to evolve in the future to match a higher slip deficit or that some asperities are not persistent over multiple events in the area of the 1960 event.

The lateral changes in locking degree apparently correlate with variations in the properties and structures of the oceanic and continental plates. In particular, the Valdivia and Mocha fracture zones encompass an area of currently reduced locking. We speculate that enhanced water circulation retards postseismic fault healing in regions above subducted fracture zones.

The locking distribution may have an expression on the long-term deformation patterns along the seismotectonic segment boundary between the 1960 and 2010 earthquakes. In this region, the area of high locking coincides with the actively deforming Arauco peninsula,

whereas the weak locking area correlates with an inflection of the coastline as well as with a topography low.

We propose that upper plate faults in the area of the Arauco peninsula may accumulate part of the plate convergence. This local deformation should reduce the slip deficit accumulation rate and thus act as a long-lived earthquake barrier controlling predominantly the seismotectonic segmentation in South–Central Chile.

Acknowledgments

Our special thanks go to Roland Bürgmann and an anonymous reviewer for their many constructive comments and suggestions. We also thank Kelin Wang and Jack Loveless for insightful comments on an early version of this manuscript. Marcos Moreno gratefully acknowledges a scholarship granted by the German Academic Exchange Service (DAAD) during part of this work. Daniel Melnick was supported by grant ME 3157/2-1 of the German Science Foundation (DFG).

Appendix A. Supplementary data

Supplementary data to this article can be found online at doi:10.1016/j.epsl.2011.03.025.

References

Alvarez, L., Saint-Amand, P., 1963. Studies made between Arauco and Valdivia with respect to the earthquakes of 21 and 22 May 1960. Bull. Seismol. Soc. Am. 53 (6), 1315–1330.

Angermann, D., Klotz, J., Reigber, C., 1999. Space-geodetic estimation of the Nazca–South America Euler vector. Earth Planet. Sci. Lett. 171 (3), 329–334. doi:10.1016/S0012-821X(99)00173-9.

Barrientos, S., Ward, S., 1990. The 1960 Chile earthquake: inversion for slip distribution from surface deformation. Geophys. J. Int. 103 (3), 589–598. doi:10.1111/j.1365-246X.1990.tb05673.x.

Bürgmann, R., Kogan, M., Steblov, G., Hilley, G., Levin, V., Apel, E., 2005. Interseismic coupling and asperity distribution along the Kamchatka subduction zone. J. Geophys. Res. 110 (B07405), 1–17. doi:10.1029/2005JB00364.

Campos, J., Hatzfeld, D., Madariaga, R., Lopez, G., Kausel, E., Zollo, A., Iannacone, G., Fromm, R., Barrientos, S., Lyon-Caen, H., 2002. A seismological study of the 1835 seismic gap in south–central Chile. Phys. Earth Planet. Inter. 132 (1–3), 177–195. doi:10.1016/S0031-9201(02)00051-1.

Cembrano, J., Herve, F., Lavenu, A., 1996. The Liquiñe-Ofqui fault zone: a long-lived intra-arc fault system in southern Chile. Tectonophysics 259 (1–3), 55–66.

Chlieh, M., Avouac, J., Sieh, K., Natawidjaja, D., Galetzka, J., 2008. Heterogeneous coupling of the Sumatran megathrust constrained by geodetic and paleogeodetic measurements. J. Geophys. Res. 113. doi:10.1029/2007JB004981.

Cisternas, M., Atwater, B., Torrejón, F., Sawai, Y., Machuca, G., Lagos, M., Eipert, A., Youlton, C., Salgado, I., Kamataki, T., Shishikura, M., Rajendran, C., Malik, J., Rizal, Y., Husni, M., 2005. Predecessors of the giant 1960 Chile earthquake. Nature 437 (7057), 404–407. doi:10.1038/nature03943.

Contreras-Reyes, E., Flueh, E., Grevemeyer, I., 2010. Tectonic control on sediment accretion and subduction off south central Chile: implications for coseismic rupture processes of the 1960 and 2010 megathrust earthquakes. Tectonics 29 (6). doi:10.1029/2010TC002734.

Contreras-Reyes, E., Grevemeyer, I., Flueh, E., Reichert, C., 2008. Upper lithospheric structure of the subduction zone offshore of the southern Arauco peninsula, Chile, at ~35°. J. Geophys. Res. 113 (B07303). doi:10.1029/2007JB005569.

Dach, R., Hugentobler, U., Fridez, P., Meindl, M., 2007. Bernese GPS Software 5.0. Astron. Inst. Univ. of Berne, Berne, Switzerland. doi:available at http://www.bernese.unibe.ch/docs/DOCU50draft.pdf.

Du, Y., Aydin, A., Segall, P., 1992. Comparison of various inversion techniques as applied to the determination of a geophysical deformation model for the 1983 Borah Peak earthquake. Bull. Seismol. Soc. Am. 82 (4), 1840–1866.

Farías, M., Vargas, G., Tassara, A., Carretier, S., Baize, S., Melnick, D., Bataille, K., 2010. Science 329 (5994), 916. doi:10.1126/science.1192094.

Glodny, J., Echtler, H., Collao, S., Ardiles, M., Buron, P., Figueroa, O., 2008. Differential Late Paleozoic active margin evolution in south-central Chile (37°–40°S) — the Lanalhue Fault Zone. J. South Amer. Earth Sci. 26, 397–4110. doi:10.1016/j.jsames.2008.06.001.

Glodny, J., Lohrmann, J., Echtler, H., Gräfe, K., Seifert, W., Collao, S., Figueroa, O., 2005. Internal dynamics of a paleoaccretionary wedge: insights from combined isotope tectonochronology and sandbox modelling of the South–Central Chilean forearc. Earth Planet. Sci. Lett. 231 (1–2), 23–39. doi:10.1016/j.epsl.2004.12.014.

Haberland, C., Rietbrock, A., Lange, D., Bataille, K., Dahm, T., 2009. Structure of the seismogenic zone of the southcentral Chilean margin revealed by local earthquake traveltime tomograph. J. Geophys. Res. 114. doi:10.1029/2008JB005802.

Haberland, C., Rietbrock, A., Lange, D., Bataille, K., Hofmann, S., 2006. Interaction between forearc and oceanic plate at the south–central Chilean margin as seen in local seismic data. Geophys. Res. Lett. 33. doi:10.1029/2006GL028189.

Harris, R., Segall, P., 1987. Detection of a locked zone at depth on the Parkfield, California, segment of the San Andreas Fault. J. Geophys. Res. 92, 7945–7962.

Hu, Y., Wang, K., He, J., Klotz, J., Khazaradze, G., 2004. Three-dimensional viscoelastic finite element model for postseismic deformation of the great 1960 Chile earthquake. Geophys. Res. Lett. 109 (12), 1–14. doi:10.1029/2004JB003163.

Kanamori, H., 1986. Rupture process of subduction-zone earthquakes. Annu. Rev. Earth Planet. Sci. 14 (1), 293–322. doi:10.1146/annurev.ea.14.050186.001453.

Kendrick, E., Bevis, M., Smalley Jr., R., Brooks, B., Vargas, R., Lauría, E., Fortes, L., 2003. The Nazca–South America Euler vector and its rate of change. J. South Amer. Earth Sci. 16 (2), 125–131.

Khazaradze, G., Wang, K., Klotz, J., Hu, Y., He, J., 2002. Prolonged post-seismic deformation of the 1960 great Chile earthquake and implications for mantle rheology. Geophys. Res. Lett. 29 (22), 7-1. doi:10.1029/2002GL015986.

Klotz, J., Khazaradze, G., Angermann, D., Reigber, C., Perdomo, R., Cifuentes, O., 2001. Earthquake cycle dominates contemporary crustal deformation in central and southern Andes. Earth Planet. Sci. Lett. 193, 437–446. doi:10.1016/S0012-821X(01)00532-5.

Konca, A., Avouac, J., Sladen, A., Meltzner, A., Sieh, K., Fang, P., Li, Z., Galetzka, J., Genrich, J., Chlieh, M., Natawidjaja, D., Bock, Y., Fielding, E., Ji, C., Helmberger, D., 2008. Partial rupture of a locked patch of the Sumatra megathrust during the 2007 earthquake sequence. Nature 456 (7222), 631–635. doi:10.1038/nature07572.

Lange, D., Cembrano, J., Rietbrock, A., Haberland, C., Dahm, T., Bataille, K., 2008. First seismic record for intra-arc strike-slip tectonics along the Liquiñe-Ofqui fault zone at the obliquely convergent plate margin of the southern Andes. Tectonophysics 455 (1–4), 14–24. doi:10.1016/j.tecto.2008.04.014.

Lay, T., Ammon, C.J., Kanamori, H., Koper, K.D., Sufri, O., Hutko, A.R., 2010. Teleseismic inversion for rupture process of the 27 February 2010 Chile (Mw 8.8) earthquake. Geophys. Res. Lett. 37 (13). doi:10.1029/2010GL043379.

Lin, J., Stein, R., 2004. Stress triggering in thrust and subduction earthquakes, and stress interaction between the southern San Andreas and nearby thrust and strike-slip faults. J. Geophys. Res. 109 (B02303). doi:10.1029/2003JB002607.

Lorito, S., Romano, F., Atzori, S., Tong, X., Avallone, A., McCloskey, J., Cocco, M., Boschi, E., Piatanesi, A., 2011. Limited overlap between the seismic gap and coseismic slip of the great 2010 Chile earthquake. Nat. Geosci. (1752-0908) dx.doi.org/10.1038/ngeo1073.

Madariaga, R., Metois, M., Vigny, C., Campos, J., 2010. Central Chile finally breaks. Science 328 (5975), 181–182. doi:10.1126/science.1189197.

Masterlark, T., 2003. Finite element model predictions of static deformation from dislocation sources in a subduction zone: sensitivities to homogeneous, isotropic, Poisson-solid, and half-space assumptions. J. Geophys. Res. 108 (B11). doi:10.1029/2002JB002296.

Melnick, D., Bookhagen, B., Echtler, H., Strecker, M., 2006. Coastal deformation and great subduction earthquakes, Isla Santa María, Chile (37°S). Geol. Soc. Am. Bull. 118 (11/12), 1463–1480. doi:10.1130/B25865.1.

Melnick, D., Bookhagen, B., Strecker, M., Echtler, H., 2009. Segmentation of subduction earthquake rupture zones from forearc deformation patterns over hundreds to millions of years, Arauco Peninsula, Chile. J. Geophys. Res. 114. doi:10.1029/2008JB005788.

Melosh, H.J., Raefsky, A., 1981. A simple and efficient method for introducing faults into finite element computations. Bull. Seismol. Soc. Am. 71 (5), 1391–1400.

Moreno, M., Rosenau, M., Oncken, O., 2010. 2010 Maule earthquake slip correlates with pre-seismic locking of Andean subduction zone. Nature 467, 198–202. doi:10.1038/nature09349.

Moreno, M.S., Bolte, J., Klotz, J., Melnick, D., 2009. Impact of megathrust geometry on inversion of coseismic slip from geodetic data: application to the 1960 Chile earthquake. Geophys. Res. Lett. 36. doi:10.1029/2009GL039276.

Moreno, M.S., Klotz, J., Melnick, D., Echtler, H., Bataille, K., 2008. Active faulting and heterogeneous deformation across a megathrust segment boundary from GPS data, south central Chile (36–39°S). Geochem. Geophys. Geosyst. 9. doi:10.1029/2008GC002198.

Murray, J., Langbein, J., 2006. Slip on the San Andreas Fault at Parkfield, California, over two earthquake cycles, and the implications for seismic hazard. Bull. Seismol. Soc. Am. 96 (4B), S283–S303. doi:10.1785/0120050820.

Murray, J., Segall, P., 2002. Testing time-predictable earthquake recurrence by direct measurement of strain accumulation and release. Nature 419, 287–291 doi.org/10.1038/nature00984.

Oleskevich, D.A., Hyndman, R.D., Wang, K., 1999. The updip and downdip limits to great subduction earthquakes: thermal and structural models of Cascadia, south Alaska, SW Japan, and Chile. J. Geophys. Res. 104 (B7), 14965–14991.

Perfettini, H., Avouac, J., Tavera, H., Kositsky, A., Nocquet, J., Bondoux, F., Chlieh, M., Sladen, A., Audin, L., Farber, D., Soler, P., 2010. Seismic and aseismic slip on the Central Peru megathrust. Nature 465, 78–81. doi:10.1038/nature09062.

Plafker, G., Savage, J., 1970. Mechanism of the Chilean earthquake of May 21 and 22, 1960. Geol. Soc. Am. Bull. 81, 1001–1030.

Prawirodirdjo, L., McCaffrey, R., Chadwell, C., Bock, Y., Subarya, C., 2010. Geodetic observations of an earthquake cycle at the Sumatra subduction zone: role of interseismic strain segmentation. J. Geophys. Res. 115 (B03414). doi:10.1029/2008JB006139.

Rehak, K., Strecker, M., Echtler, H., 2007. Morphotectonic segmentation of an active forearc, 37°–41°S, Chile. Geomorphology 94, 94–116. doi:10.1016/j.geomorph.2007.05.002.

Rosenau, M., Melnick, D., Echtler, H., 2006. Kinematic constraints on intra-arc shear and strain partitioning in the Southern Andes between 38°S and 42°S latitude. Tectonics 25 (4), TC4013. doi:10.1029/2005TC001943.

Rosenau, M., Oncken, O., 2009. Fore-arc deformation controls frequency-size distribution of megathrust earthquakes in subduction zones. J. Geophys. Res. 114, B10311. doi:10.1029/2009JB006359.

Ruegg, J.C., Rudloff, A., Vigny, C., Madariaga, R., Dechabalier, J., Campos, J., Kausel, E., Barrientos, S., Dimitrov, D., 2009. Interseismic strain accumulation measured by GPS in south central Chile seismic gap. Phys. Earth Planet. Inter. 175 (1–2), 78–85. doi:10.1016/j.pepi.2008.02.015.

Satake, K., Fujii, Y., 2010. Seismic moment and slip distribution of the 1960 and 2010 Chilean earthquakes as inferred from tsunami waveforms. Presented at 2010 Fall Meeting, AGU. G31B-02, San Francisco, Calif., 13–17 Dec.

Savage, J., 1983. A dislocation model of strain accumulation and release at a subduction zone. J. Geophys. Res. 88 (B6), 4984–4996.

Shimazaki, K., Nakata, T., 1980. Time-predictable recurrence model for large earthquakes. Geophys. Res. Lett. 7 (4), 279–282.

Song, T.R.A., Simons, M., 2003. Large trench-parallel gravity variations predict seismogenic behavior in subduction zones. Science 301 (5633), 630–633. doi:10.1126/science.1085557.

Suito, H., Freymueller, J.T., 2009. A viscoelastic and afterslip postseismic deformation model for the 1964 Alaska earthquake. J. Geophys. Res. 114 (B11). doi:10.1029/2008JB005954.

Tassara, A., Götze, H., Schmidt, S., Hackney, R., 2006. Three-dimensional density model of the Nazca plate and the Andean continental margin. J. Geophys. Res. 111 (B09404). doi:10.1029/2005JB003976.

Tebbens, S., Cande, S., 1997. Southeast Pacific tectonic evolution from early Oligocene to present. J. Geophys. Res. 102 (B6), 12061–12084. doi:10.1029/96JB02582.

Tong, X., Sandwell, D., Luttrell, K., Brooks, B., Bevis, M., Shimada, M., Foster, J., Smalley, R., Parra, H., Baez, J.C., Blanco, M., Kendrick, E., Genrich, J., Caccamise, D., 2010. The 2010 Maule, Chile earthquake: downdip rupture limit revealed by space geodesy. Geophys. Res. Lett. 37. doi:10.1029/2010GL045805.

Walcott, R.I., 1978. Geodetic strains and large earthquakes in the axial tectonic belt of North Island, New Zealand. J. Geophys. Res. 83. doi:10.1029/JB083iB09p04419.

Wang, K., Hu, Y., Bevis, M., Kendrick, E., Smalley Jr., R., Barriga-Vargas, R., Lauría, E., 2007. Crustal motion in the zone of the 1960 Chile earthquake: detangling earthquake-cycle deformation and forearc-sliver translation. Geochem. Geophys. Geosyst. 8 (Q10010). doi:10.1029/2007GC001721.

Wells, R., Blakely, R., Sugiyama, Y., Scholl, D., Dinterman, P., 2003. Basin-centered asperities in great subduction zone earthquakes: a link between slip, subsidence, and subduction erosion? J. Geophys. Res. 108 (B10), 1–16. doi:10.1029/2002JB002072.